JOURNAL OF PROPULSION AND POWER
Vol. 25, No. 2, March–April 2009

Measurement of Flow Properties and Thrust on Scramjet Nozzle Using Pressure-Sensitive Paint

C. Hirschen,* A. Gülhan,† W. H. Beck,‡ and U. Henne§
DLR, German Aerospace Center, 51147 Cologne, Germany

DOI: 10.2514/1.37957

An experimental study of flows over a single expansion ramp nozzle with flush-mounted side walls was carried out at the DLR, German Aerospace Center. The tests were performed at a freestream Mach number of 7 in the hypersonic wind tunnel H2K in Cologne. The Reynolds number and nozzle pressure ratios in the wind-tunnel flow were varied to study the performance of the scramjet nozzle at different flight altitudes and run conditions. The static pressure distribution on the single expansion ramp was measured by both the pressure-sensitive paint method and by using pressure transducer taps located at discrete points on the surface. These two methods showed that the nozzle pressure ratio and the freestream Reynolds number do not substantially influence the static pressure ratio on the expansion ramp. A pitot rake was also used to measure the pressure distribution in the nozzle wake. Using this technique the nozzle flow in the wake could be visualized and the strong influence of the nozzle pressure ratio on the interaction between nozzle and external flows was revealed. The data obtained by the different measurement techniques permitted a characterization of the nozzle flow and gave insight into the properties of single expansion ramp nozzle flows. The thrust generated by the nozzle, the thrust efficiency coefficient, and the thrust vector angle were calculated by using the pressure data obtained by both pressure measurement techniques and the results compared. It was shown that thrust values obtained from pressure tap measurements were overestimated. Criteria were developed to aid in the design and optimization of the thrust-related performance criteria for this single ramp nozzle.

Nomenclature

A = area, m^2
b = width of nozzle, m
c_{fg} = thrust efficiency coefficient, –
F = force, N
h = height of nozzle entrance, m
Ma = Mach number, –
n = direction normal to the surface
p = pressure, $\mathrm{N} \cdot \mathrm{m}^{-2}$
R = general gas constant, 287 $\mathrm{m}^2 \cdot \mathrm{s}^{-2} \cdot \mathrm{K}^{-1}$ for air
Re_U = unit Reynolds number, m^{-1}
T = temperature, K
t = time, s
x = streamwise distance from nozzle entry, mm
y = spanwise direction from nozzle centerline, mm
z = height above or below flap (see Fig. 4), mm
α = angle of attack, deg
β_f = thrust vector angle, deg
γ = heat capacity ratio, –
Δx = ratio between PSP and PSI calculated thrust forces, –
Δz = ratio between PSP and PSI calculated lift forces, –
Π = nozzle pressure ratio, $\Pi = p_{0,N}/p_{\infty}$, –
ρ = density, $\mathrm{kg} \cdot \mathrm{m}^{-3}$

Subscripts

A = exit plane of nozzle
E = entrance plane of nozzle
id = ideal
N = nozzle conditions
stat = static
t = total conditions
tot = total force
x, y, z = coordinate directions
0 = total conditions
∞ = wind-tunnel freestream conditions
$*$ = sonic condition

I. Introduction

AIRBREATHING propulsion is an alternative to the existing rocket propulsion systems which carry their oxidant (e.g., liquid oxygen) on board [1–3]. This saves weight and allows larger payloads. Aerodynamic stability and generation of sufficient thrust are major problems of a hypersonic vehicle with scramjet propulsion, whereby the nozzle and external base flow interactions play a large role [4]. Although the interaction of the hypersonic nozzle/afterbody flowfield with a cold plume flow has been extensively studied [5–7], there is still a lack of experimental data. It is therefore necessary to study the aerodynamic phenomena which arise from the interaction between the outer base flow and the hot nozzle flow, and to understand their effects on the nozzle performance. This interaction is mainly driven by temperature, viscosity, and heat capacity ratio effects.

The dynamic interactions between the aerodynamics of the vehicle and the thrust have also been studied numerically [8,9]. Ebrahimi [10] introduced an efficient design code for scramjet nozzle design. Ishiguro et al. in [11] show the results of a three-dimensional analysis of scramjet nozzle flows which agree well (in certain aspects) with the experimental results. In [12] the effects on the flow interaction of employing simulant gases instead of air for the scramjet nozzle flow are presented. Experimental studies investigating the interactions between the external flow and internal nozzle flow have been shown to be very complex and not fully understood as yet [13–15]. In [16] a broad experimental study on the boundary-layer effects in a scramjet

---

Received 8 April 2008; revision received 25 November 2008; accepted for publication 25 November 2008.

*Ph.D. Student, Wind Tunnel Department, Institute of Aerodynamics and Flow Technology, Linder Höhe. Student Member AIAA.

†Head of Department, Wind Tunnel Department, Institute of Aerodynamics and Flow Technology, Linder Höhe. Member AIAA.

‡Research Scientist, Experimental Methods Department, Institute of Aerodynamics and Flow Technology, Bunsenstraße 10 D-37073 Göttingen. Senior Member AIAA.

§Research Scientist, Experimental Methods Department of Institute of Aerodynamics and Flow Technology, Bunsenstraße 10 D-37073 Göttingen.

nozzle has been carried out. These experimental and numerical studies, however, point to the necessity of further research in this field.

As part of a research project that aims at improving the key technologies for the design of a scramjet propulsion unit [17], the goal of the present study is to investigate the flow of a generic 2-D scramjet nozzle and carry out an experimental study of its performance. Mitani et al. [18] performed an experimental study on the performance of a scramjet nozzle, where they compared the experimental data with the results obtained by an inviscid two-dimensional chemical kinetic code. They showed that lift thrust and main thrust are comparable and very sensitive to the nozzle configuration.

In a previous experimental study [19] with a three-dimensional single expansion ramp nozzle, extensive measurements using the pressure-sensitive paint (PSP) technique, a pitot probe rake, and surface pressure taps in the nozzle ramp had been carried out. Reasonable to good agreement between PSP and surface pressure tap values was obtained, although the presence of an asymmetry in the pressure distribution on the ramp, seen by both methods (PSP and pressure taps), could be attributed to side injection of the gas for the internal nozzle flow into the plenum upstream of the nozzle ramp. In spite of this, it could still be demonstrated that a meaningful physical interpretation of the flow and its interactions with the surrounding flow could be obtained. Therefore, in this present work, a different injection mode has been designed, bringing the gas in from top and on the centerline into the model plenum. Furthermore, a simpler 2-D geometry of the nozzle ramp was chosen, and the side walls, present in the first model, were flush mounted with the ramp (see Sec. II.B, Fig. 2a). One of the objectives of the present study was to gain information about both the nozzle flow of this two-dimensional single expansion ramp nozzle [which had been designed according to the method of characteristics [20]] and also its interaction with the external flow. Furthermore, the effects of the different position of gas injection into the test model are investigated.

The influence of the heat capacity ratio, nozzle pressure ratio, and freestream Reynolds number on the flow of a three-dimensional single expansion ramp nozzle has already been investigated (see [21,22]). Therefore, as in the previous study, different measurement techniques are applied here to gain further information of the flowfield and the thrust generated by the nozzle. The different measurement techniques enable the visualization of different flow aspects such as shock positions, shear layer position, and surface pressure, as well as exhaust plume shape. Shock and shear layer position as well as the shape of the exhaust plume were measured and “visualized by means” of pitot pressure measurements. The surface pressure distribution is obtained by pressure static measurements (using embedded sensors) and the PSP method. This latter method allows the measurement of the pressure distribution on a large part of the model surface and therefore gives more information than the static pressure measurements at discrete points alone. Previous experimental studies have demonstrated the applicability of the PSP technique to supersonic flow regimes [21,22] and to the H2K hypersonic wind-tunnel facility at the DLR in Cologne [19]. In this work this application to H2K is continued and the various test techniques are applied to a different single expansion ramp nozzle model, which is at present under study in a new scramjet project in Germany [23].

A major goal of this present work is to evaluate the performance of this single expansion ramp nozzle with respect to its generated thrust. (As in the first study [20,22], only cold gas injection without combustion has been used here.) The thrust generated by the single expansion ramp nozzle was determined from both the Pressure System Incorporation (PSI) and the PSP pressure measurements and the results compared. This comparison enables one to estimate the inaccuracies obtained if the thrust has been determined using only the PSI sensors at discrete points on the ramp surface. The thrust coefficient and the thrust vector angle were calculated for different flow conditions, obtained by running the H2K tunnel at different nozzle pressure ratios Π and freestream Reynolds numbers Re_U. The effects of these two parameters on the thrust, thrust coefficient, and thrust vector angle were investigated, thus aiding in ascertaining the optimal flow configuration to generate positive net thrust and hence to accelerate the vehicle.

These experiments were performed at a freestream Mach number $Ma_\infty = 7$ and Reynolds numbers of $Re_U = 4.0 \times 10^6$ and $Re_U = 8.0 \times 10^6$ to simulate different flight altitudes, viz., 30 and 25 km, respectively. According to former experimental studies, the nozzle pressure ratio Π and the freestream Reynolds number Re_U are the main parameters affecting the nozzle flow behavior [24–26]. The experimental results obtained by the pitot pressure measurements and the PSP method are compared to gain complementary information about the flow properties, the pressure distributions, and the thrust of this scramjet nozzle.

II. Experimental Methods

A. Wind Tunnel and Test Conditions

The experiments were carried out in the H2K hypersonic wind-tunnel facility of the DLR, German Aerospace Center in Cologne, which has been described in more detail elsewhere [27]. In brief, this facility is a blowdown wind tunnel with test durations of up to 30 s, depending on the flow conditions. For these experiments, the Mach 7 nozzle was used. The unit Reynolds number is given by the proper choice of the total pressure p_0 and T_0 of the flow. A schematic sketch of the hypersonic wind-tunnel facility is shown in Fig. 1. The wind-tunnel flow conditions for these tests with the nozzle model are summarized in Table 1; the accuracy of measurement is as follows: $\Delta M/M = 0.50\%$, $\Delta T_0/T_0 = 0.75\%$, and $\Delta p_0/p_0 = 0.02\%$.

B. Model and Experimental Setup

Experiments with a single expansion ramp nozzle (SERN) equipped with a generic forebody (see Fig. 2) were carried out. The wind-tunnel model was designed in a modular way so that the single components of the model can be exchanged, providing an easy means of examining parametric and geometric variations. The single expansion ramp nozzle (Fig. 2b) was designed using an in-house tool to match the conditions (in terms of pressure and Mach number) at the end of the combustion chamber of a scramjet vehicle. For these tests the model and tunnel axes were aligned in parallel.

To provide a uniform flow, a honeycomb followed by a contoured 2-D Laval nozzle (Fig. 2b) was installed inside the settling chamber. The Laval nozzle was necessary to provide supersonic flow and to match the appropriate Mach number at the combustor exit, which was $Ma = 2$ for these experiments. The entrance to the single expansion ramp nozzle has a cross-sectional area of 20 mm height × 80 mm width.

The model is a 2-D single expansion ramp nozzle (see Fig. 3) with a total length of 200 mm and a total width of 80 mm. The nozzle is equipped with 26 pressure taps (orifices) in total. There are four on the cowl, and 22 on the ramp, being placed along three different lines in the flow direction. Fourteen are on the centerline, four are displaced 35 mm to the right side, and four are displaced 20 mm to the left side of the centerline (see Fig. 3), as seen when looking down the nozzle in the flow direction. In Fig. 3 the positions of the pressure orifices are marked by the black dots.

Figure 4 shows the entire model installed in the wind-tunnel section (flow is from left to right). It can be seen that the model is held by a vertical strut that is mounted onto the side of the model and connected to it by an adapter to attain a certain separation between the

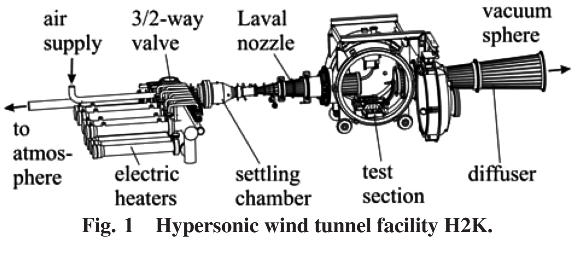

Fig. 1 Hypersonic wind tunnel facility H2K.

Table 1 Wind-tunnel flow conditions

Flow properties	Wind-tunnel condition I	Wind-tunnel condition II
Freestream Mach number Ma_∞, –	7	7
Freestream pressure p_∞, Pa	260	515
Freestream temperature T_∞, K	60	60
Freestream density ρ_∞, $\mathrm{kg/m^3}$	0.015	0.029
Total temperature T_0, K	650	650
Total pressure p_0, Pa	10×10^5	21×10^5
Unit Reynolds number Re_U, 1/m	4×10^6	8×10^6

strut and the model. This separation prevents the shock originating from the strut leading edge from perturbing the nozzle flowfield. The angles of attack and yaw were not varied and set here to 0 deg.

The exhaust gas (nozzle internal flow) was supplied to the nozzle plenum by a pipe, which was connected to the plenum at the beginning of the settling chamber at one end and to a tube at the other end, through which the test gas, which is stored in an external separate reservoir near the wind tunnel, was injected. In the previous experimental study [19], the pipe had been connected to the side of the forebody, which resulted in the measured asymmetric pressure distributions described before. To avoid this asymmetry and improve the quality of the flow, the pipe is now connected on the centerline on top of the settling chamber.

C. Measurement Techniques

During the experiments the jet total pressure $p_{0,N}$ and total temperature $T_{0,N}$ are measured with a pitot tube and a thermocouple in the settling chamber downstream of the honeycomb and upstream of the internal Laval nozzle. The static pressures on the single expansion ramp nozzle are measured with a PSI module with the range of 15 psi (∼105 kPa).

1. *Pitot Pressure Measurements*

To obtain a pressure distribution of the flowfield, pitot pressure measurements were carried out. The pitot rake had 14 pitot probes placed 6 mm apart, leading to a total pitot rake span of 79 mm. To measure the pitot pressure distribution in the entire flowfield, the pitot rake is displaced in axial (x) and vertical (z) directions. Figure 5 shows the displacement unit; the coordinate system used is also shown. The pitot rake is mounted to a rod which is moved in a vertical direction by a linear motor, and a potentiometer is used to measure its position. The entire unit of potentiometer, rod, and pitot rake can be moved in the x (flow) direction. The measurement of the pitot pressure at different z and x positions enables a mapping of the flow over and downstream of the nozzle. The achieved spatial resolution of this process depends on the adopted step sizes in the z and x directions: here $\Delta z = 2$ mm and $\Delta x = 30$ mm were used. Hence, for each x position a grid of points in the y–z plane is measured; with $\Delta y = 6$ mm and $\Delta z = 2$ mm as the grid spacing, the representation as a continuous flowfield can be obtained by interpolating between the discrete points.

The pitot tubes are also connected to a PSI module with the same operating range of 15 psi, which records and then digitizes the pressure values in a scanner interface, from where they are sent to a computer. For more details on how the pitot measurements are carried out and how the flow properties are ascertained, see [19,25].

2. *Pressure-Sensitive Paint Method*

The PSP measurement technique as used here is based on the photochemical deactivation by oxygen molecules of excited (paint)

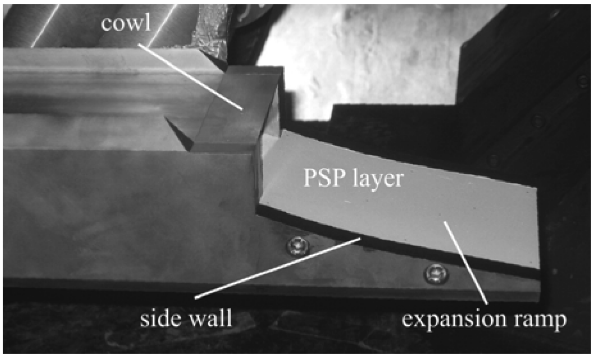

a) Model in wind tunnel

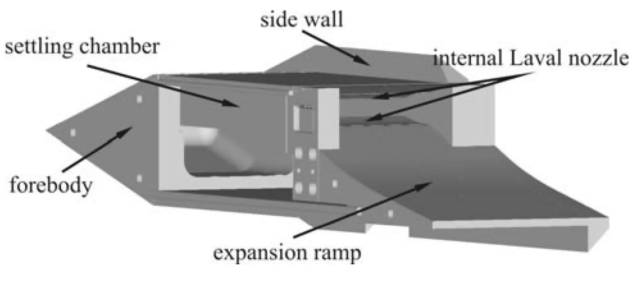

b) 3-D sketch of modular model

Fig. 2 Forebody and nozzle.

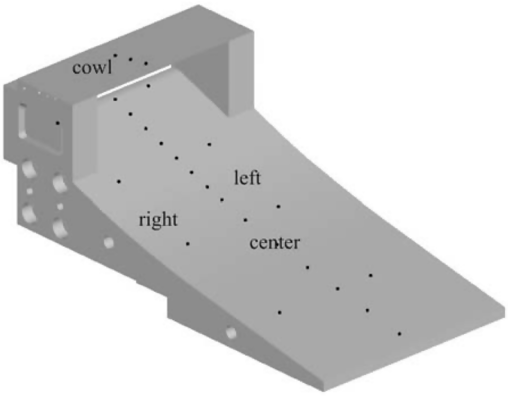

Fig. 3 Pressure orifices of the two-dimensional single expansion ramp nozzle.

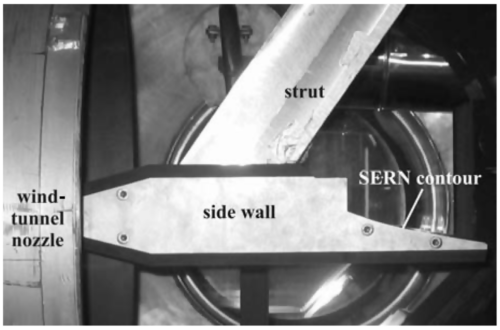

Fig. 4 Side view of the nozzle model connected to a forebody.

molecules called luminophores. When these luminophores absorb UV light, the intensity of their fluorescence at higher wavelengths is dependent on the concentration of oxygen (viz., air) in their surroundings [28]. As in the previous study [19,25], the DLR02 paint formulation has been used. Excitation in the UV is from a flash lamp operating at 20 Hz, and fluorescence of the pressure-dependent and pressure-independent components of the paint occurs at 450–550 and 600–650 nm, respectively. Two cooled PCO charge-coupled device (CCD) cameras with 12-bit resolution and exposure times of 1.7 s were used for image acquisition; hence, at 20 Hz, the fluorescence arising from about 34 flash lamp pulses was cumulatively stored on the CCD chips, leading to an averaging of the pressure levels over this time window. By using filters in front of the cameras, the one camera captured only the pressure-sensitive signal and the other only the reference pressure-insensitive signal.

A calibration of the optical pressure sensor is carried out in situ in the wind tunnel and on separate samples in a PSP calibration chamber where both temperature and pressure can be varied. The temperature of the model surface in the H2K wind tunnel was measured before, during, and after the experiment using a Thermacam 3000 (FLIR Systems) infrared (IR) camera. An overview of the PSP setup is shown in Fig. 6. More details on the PSP technique, as used here, are given in [19,25].

The various sources of measurement uncertainty in the PSP measurements were discussed in the previous study [19]. Using a similar approach here, the total uncertainty from all sources was estimated as the square root of the summed squares of the individual errors. By far the largest contribution comes from the (known) variation in temperature over the nozzle ramp surface, which is ±6 K (this corresponds to an error in pressure, when using just a single, average temperature for the whole surface, of ±2.1% for the measured temperature range, based on the temperature dependence of this paint as determined in the calibration chamber). The total error for PSP is about 5%.

III. Experimental Results and Discussion

A. Flow Properties of the Single Expansion Ramp Nozzle

1. PSP Results

Figure 7 shows the normalized static pressure distribution obtained by the PSP method for a freestream Reynolds number of $Re_U = 8 \times 10^6$ and a nozzle pressure ratio of $\Pi = 500$; also shown are the positions of the pressure orifices on the left, center, and right lines (as described before in Sec. II.B) and the characteristic lines of the expansion fan (from the calculation). The PSP pressures could only be measured at $x \geq 20$ mm, due to the limited optical access farther upstream. Figures 8a–8c compare the PSP measurements along the three lines with the PSI values. Only two PSI values for the left line, Fig. 8c, are shown, because the last sensor in this line had malfunctioned during the tests. For the data obtained with the PSI transducers, the error is ±0.15% of the full scale pressure range of the used PSI module, leading to a measurement uncertainty here of ±1.55 mbar. Therefore, the error bars for the PSI measurement are of the size or smaller than the symbols representing their values in these figures. Representative PSP error bars are shown in Fig. 8a. All pressures are plotted normalized to the total nozzle pressure $p_{0,N}$.

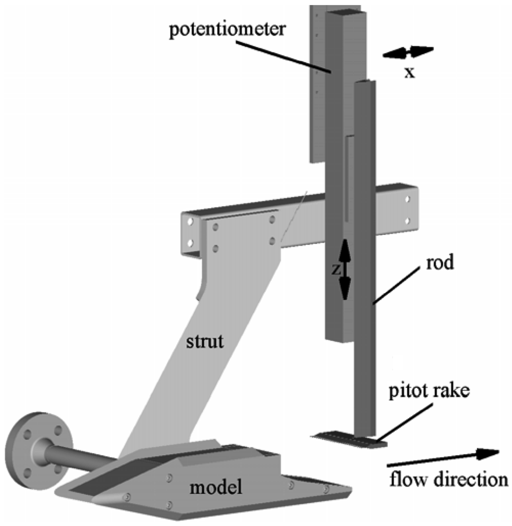

Fig. 5 Pitot rake displacement unit.

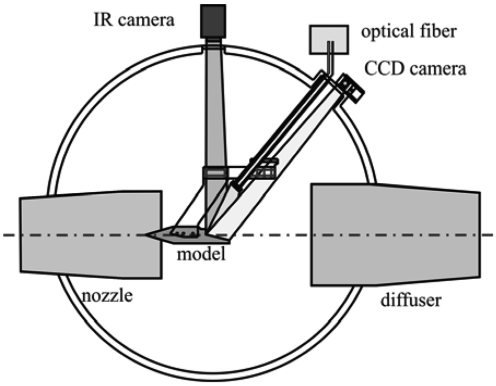

Fig. 6 Setup for PSP.

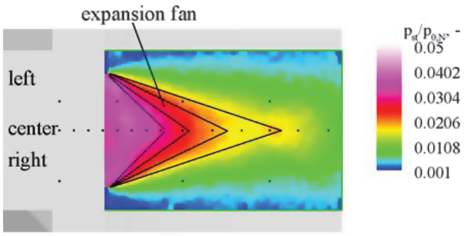

Fig. 7 PSP measurement results for $Re_U = 8 \times 10^6$ and $\Pi = 500$.

Figure 7 shows that the flowfield is fully established and symmetric in the y direction, confirming the improvement brought about by the top injection position used here. Figures 8a–8c also show the excellent agreement between the PSI and PSP measurements for all three lines (center, left, and right). Whereas in the previous measurements [19] the agreement between PSP and PSI values had not been equally good over the total range of x, an effect which at that time could not be fully explained, in this experimental study the agreement is excellent over the whole range of points. [A likely reason for the improvement here is the optimization of the positioning of the excitation (light) source relative to the model, leading to a more evenly distributed radiation over the whole model surface.]

Figures 8b and 8c show the typical pressure distribution expected for a single expansion ramp nozzle: a high pressure region at the beginning of the ramp followed by a sudden decrease of the pressure due to the 3-D expansion. The two regions (high and low pressure) are separated by a pressure plateau between about $x = 25$–50 mm. The reason for this is that the slope of the nozzle contour is constant in this region; hence the flow is not further accelerated in the x direction in this region. The different rates of pressure drop in Figs. 8b and 8c are due to the different positions in the y direction of the two lines of pressure orifices: the values from those sensors which are farther from the centerline (viz., left line at $y = 35$ mm) exhibit a more rapid drop in the x direction due to the 3-D expansion being stronger there.

a. Influence of Nozzle Pressure Ratio. Figures 9 and 10 show the influence of the nozzle pressure ratio Π on the pressure distribution on the surface of the single expansion ramp: depicted are the normalized pressure distributions for nozzle pressure ratios $\Pi = 250$ and 375, both at a freestream Reynolds number of $Re_U = 8 \times 10^6$. The result of varying Π can be seen to be very small. The pressure distribution over the surface is quite remarkable, because, in fact, this single expansion ramp nozzle had been designed

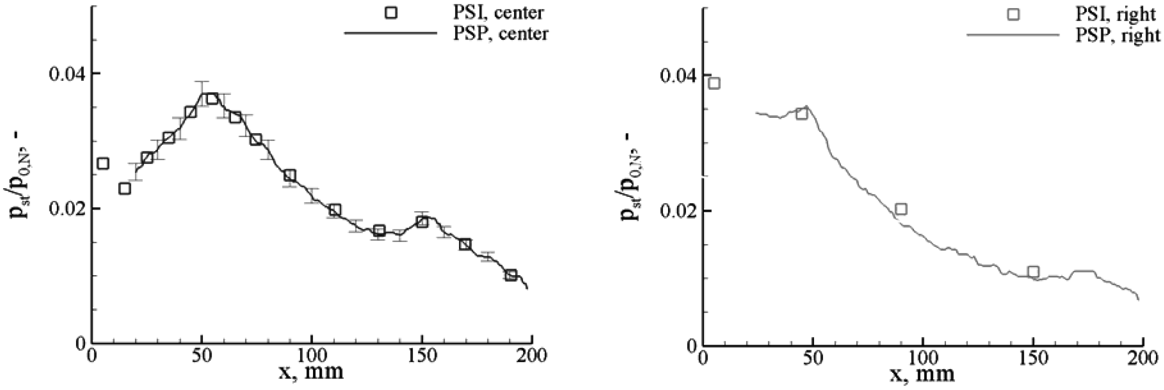

a) Distribution for centerline

b) Distribution for right line

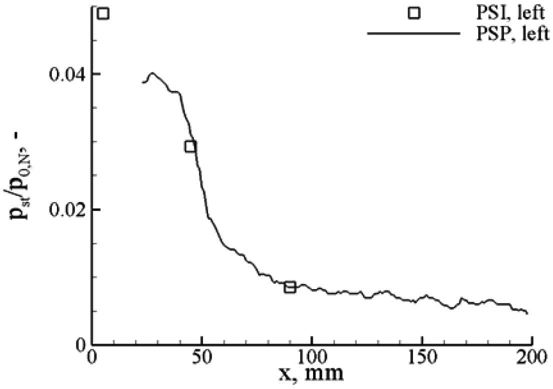

c) Distribution for left line

Fig. 8 Comparison between PSI and PSP pressure measurements for $Re_U = 8 \times 10^6$ and $\Pi = 500$.

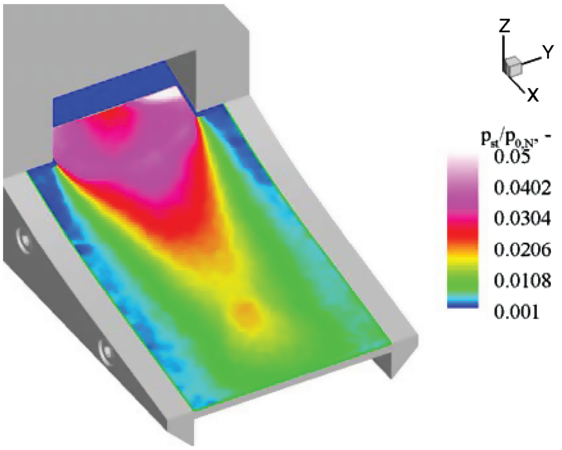

Fig. 9 PSP pressure measurements for $Re_U = 8 \times 10^6$ and $\Pi = 250$.

to be 2-D. Because the pressure pattern mirrors the flow pattern, however, it is obvious that the nozzle flow here is highly three dimensional. It can be seen that due to the 3-D expansion the pressure decreases not only in the streamwise (x), but also in the spanwise (y) direction, revealing the typical pattern of an expansion fan at both upper corners of the sides. The Mach number behaves in an opposite way to the pressure: high/low pressures indicate low/high Mach numbers, respectively. This measured pressure distribution is as expected: the flow along the freestream boundary of the exhaust plume in the y direction accelerates more strongly than inside the exhaust plume.

In the x direction the pressure level also decreases due to the expansion of the flow. The pressure, however, suddenly increases at one point, where a higher pressure plateau (at around $x = 150$ mm and $y = -5$ to 5 mm) is found. This plateau along the centerline is most likely caused by the interactions of the characteristics originating at the entrance of the nozzle and reflected at the freestream boundary of the exhaust plume with the flow along the expansion ramp (see Fig. 11).

The pressure distribution along the y direction is plotted in Fig. 12 for different streamwise (x direction) positions. At $x = 50$ mm the pressure plateau is very broad, with the width of the plateau in the y direction decreasing as one moves farther downstream in the x direction. The reason for this behavior is the aforementioned 3-D expansion that decreases the pressure in both the x and the y directions. At $x = 150$ mm the peak of the pressure distribution due to the above-mentioned interactions of the characteristics with the expansion ramp flow can be clearly seen. Downstream of this

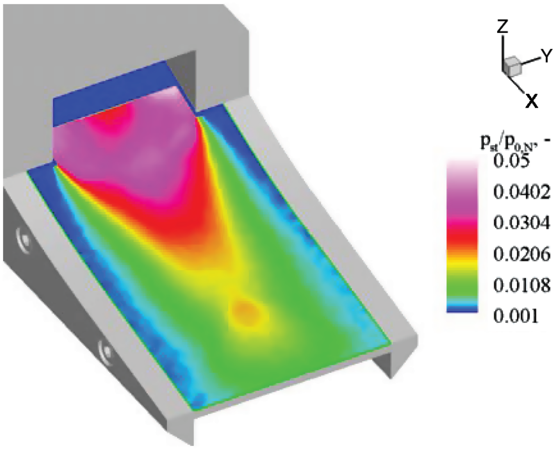

Fig. 10 PSP pressure measurements for $Re_U = 8 \times 10^6$ and $\Pi = 375$.

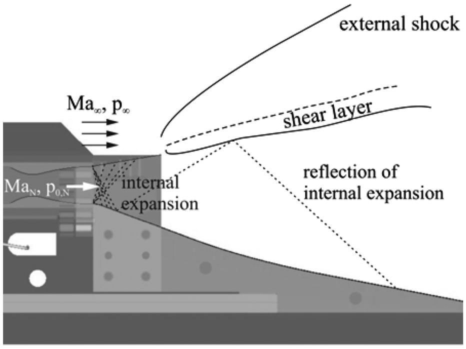

Fig. 11 Schematic of nozzle flow and characteristics originating at entrance of nozzle.

position the pressure distribution is very flat again, not having a discernible single peak. In comparison between the pressure distributions for the two nozzle pressure ratios $\Pi = 250$ and 375, Figs. 12 and 13 once again exemplify that the pressure distribution is little affected by a variation of Π.

This similarity can be more clearly seen in a comparison of the pressure distributions for two different combinations of Π/Re_U ($500/8 \times 10^6$ and $1000/4 \times 10^6$), as shown in the pressure field plot of Fig. 14 and the sections across the pressure field in Fig. 15. In both cases the same nozzle total pressure $p_{0,N} = 2.6$ bar applies. As can clearly be seen, the differences in both figures are very small. This result shows again that the normalized pressure distribution is independent of the nozzle pressure ratio. Therefore, the pressure distribution for any nozzle pressure ratio can be easily obtained by multiplying the normalized pressure distribution, obtained for a certain nozzle pressure ratio, with the corresponding nozzle total pressure. The pressure distribution on the expansion ramp does not depend on the external flow, but only depends on the nozzle total pressure, which then determines the overall gross thrust obtained. The drag of the exhaust plume, however, is influenced by the nozzle pressure ratio.

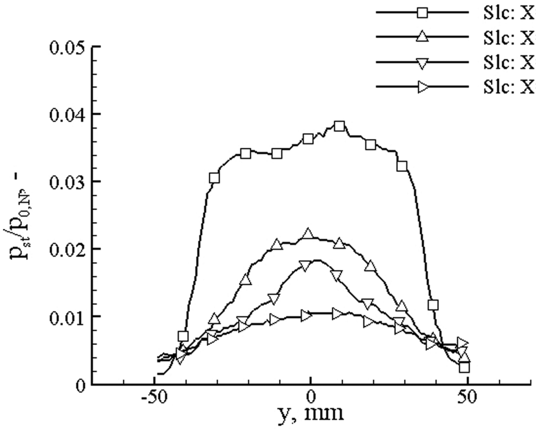

Fig. 12 Pressure slices in the *y* direction at different streamwise positions for $Re_U = 8 \times 10^6$ and $\Pi = 250$.

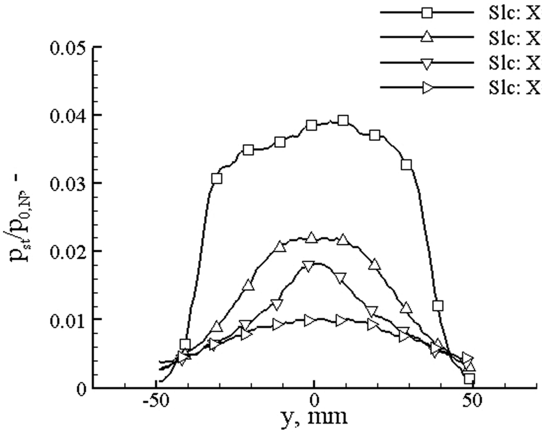

Fig. 13 Pressure slices in the *y* direction at different streamwise positions for $Re_U = 8 \times 10^6$ and $\Pi = 375$.

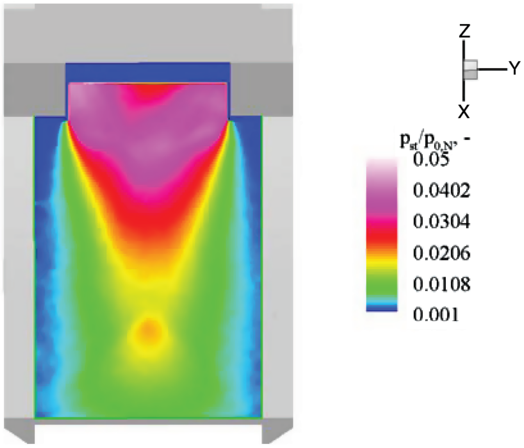

Fig. 14 Comparison of PSP pressure measurements for $Re_U = 8 \times 10^6$ and $\Pi = 500$ (on the left side of the ramp) as well as $Re_U = 4 \times 10^6$ and $\Pi = 1000$ (on the right side of the ramp).

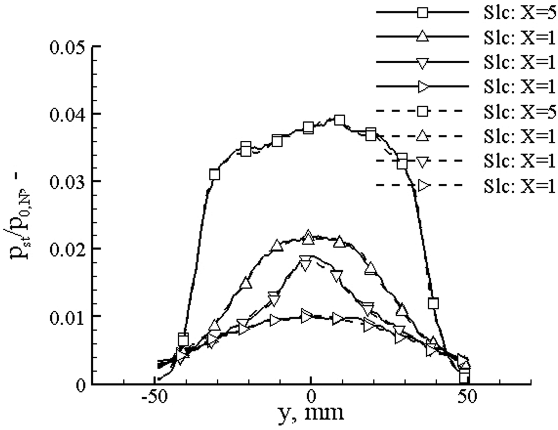

Fig. 15 Comparison of PSP pressure measurements for $Re_U = 8 \times 10^6$ and $\Pi = 500$ (solid lines) as well as $Re_U = 4 \times 10^6$ and $\Pi = 1000$ (dashed lines).

b. Influence of the Freestream Reynolds Number. The influence of the freestream Reynolds number has also been investigated. From previous experimental studies [19] it is known that the influence of the freestream Reynolds number is fairly small for underexpanded nozzles. But due to the fact that this new 2-D nozzle had been designed with flush-mounted side walls, it was expected that there may be some influence of the external flow on the nozzle flow. Figures 16 and 17 show the pressure distribution for $\Pi = 500$ and for two different freestream Reynolds numbers $Re_U = 4 \times 10^6$ and 8×10^6. As can be clearly observed, the influence of Re_U on the pressure distribution is barely detectable and almost certainly negligible. This observation supports the above statement that the pressure distribution and thus the gross thrust depend mainly on the nozzle total pressure. The flow pattern, however, seems to be fully independent of the flow parameters and only dependent on geometry parameters such as the nozzle contour in the investigated region. Figure 18 shows a comparison of pressures for the two different freestream Reynolds numbers in the spanwise direction at different streamwise locations. The solid lines represent the results for $Re_U = 4 \times 10^6$ and the dashed lines for $Re_U = 8 \times 10^6$. Small differences in normalized pressure are seen only at a streamwise

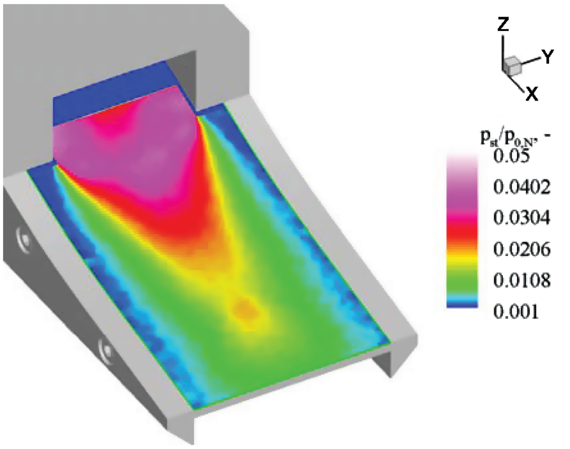

Fig. 16 **PSP pressure measurements for $Re_U = 4 \times 10^6$ and $\Pi = 500$.**

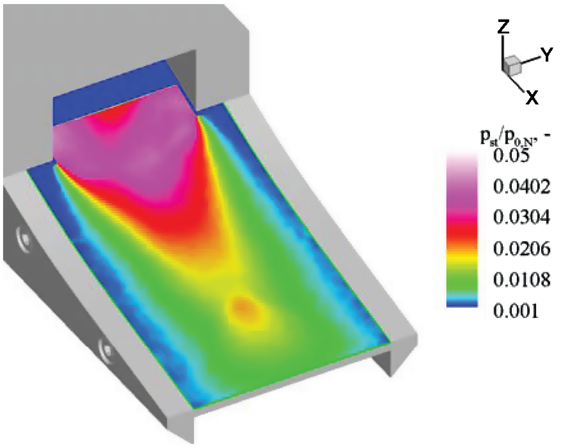

Fig. 17 **PSP pressure measurements for $Re_U = 8 \times 10^6$ and $\Pi = 500$.**

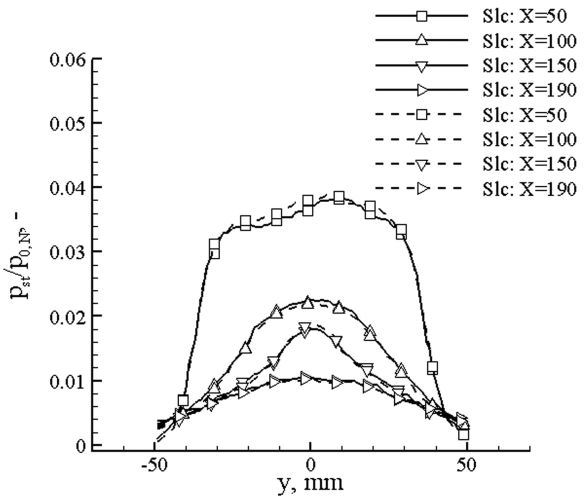

Fig. 18 **Comparison of PSP pressure measurements for $\Pi = 500$ and two different freestream Reynolds number $Re_U = 8 \times 10^6$ (solid lines) and $Re_U = 4 \times 10^6$ (dashed lines).**

position of $x = 50$ mm, whereas at other larger values of x they coincide almost exactly. The independency from the Reynolds number on the pressure distribution was also found for symmetrical rocket nozzles in [29].

The PSP results obtained here show again that this technique is a useful way of visualizing the pressure distribution on the entire surface of this scramjet nozzle, aiding in the detection and understanding of the flow phenomena in a better way than pressure measurements using only the PSI sensors alone could have provided. The excellent agreement with the PSI pressure measurements showed that a qualitatively and quantitatively correct pressure distribution for the scramjet nozzle could be obtained. PSP clearly reveals more information about the flowfield than local PSI pressure measurements and allows a better assessment of the nozzle flow. For complicated model geometries the thrust can be calculated more easily and accurately by the pressure-sensitive paint method than by local PSI pressure measurements [28], see also Sec. III.B.

2. *Pitot Pressure Measurements*

Pitot pressure measurements have also been carried out to obtain 3-D spatial information of the flowfield in the wake of the nozzle. The pitot rake was mounted at a downstream position $x = 220$ mm, that is, 20 mm downstream of the nozzle, thereby enabling the influence of varying Re_U and Π on the nozzle flow and on the interactions with the external flow to be measured. Figures 19a–19c show the results of the pitot pressure measurements with the rake at $x = 220$ mm and at the one value of $Re_U = 8 \times 10^6$, but at three different values of Π, viz., 500, 250, and 191. It can be seen that the nozzle flow in the wake of the nozzle is not independent of the nozzle pressure ratio, with the pitot pressure varying significantly in the upper region of the measured field at positions $z \geq 25$ mm.

The high pressure region between $y = -40$ to $+40$ mm and $z = -70$ to -40 mm is very similar in all three cases. The nozzle flow along the wall of the ramp seems to be independent of the nozzle pressure ratio, a result which was revealed by the PSP pressure measurements presented earlier and now confirmed by the pitot pressure measurements. However, in other regions farther away from the wall, the results differ markedly. The reason for this is the differing nozzle pressure ratio and the resulting different interactions with the external flow. The nozzle pressure ratio influences the size of the exhaust plume which then in turn affects the external flow itself. Because of the stronger expansion of the flow for higher nozzle pressure ratios, for example, $\Pi = 500$ in Fig. 20a, the exhaust plume becomes enlarged in the z and y directions and thereby displaces the external flow more than in the cases of lower nozzle pressure ratios. Therefore, the influence of the external flow on the nozzle flow can already be seen for the lower nozzle pressure ratios $\Pi = 250$ and $\Pi = 191$, where higher pressures in the upper region can be seen (this is especially so in the top right corner, $z \sim 0$ mm, $y \sim +30$ mm).

As previously stated, higher pitot pressures usually indicate lower Mach numbers (and vice versa). For $\Pi = 500$ the lowest pitot pressures are to be found at the top right- and left-hand corners as well as at the very bottom. These low pressure regions help to identify the positions of the freestream boundaries of the exhaust plume, where the largest flow acceleration occurs. In the case of $\Pi = 500$ the flow expands at the end of the nozzle so strongly that the exhaust plume is still within the measurement plane at the streamwise position $x = 220$ mm. This is not the case for the other two nozzle pressure ratios as can be seen from the pitot pressure values. At this streamwise position the influence of the external flow on the nozzle flow is already detectable at the lower and upper regions due to the fact that the exhaust plume in the y and z directions is smaller and thus the displacement of the external flow. It seems that the boundaries (shear layer) of the exhaust plume are visible inside the measurement plane for the lower nozzle pressure ratios, whereas for $\Pi = 500$ the boundaries are still located outside the measurement plane and therefore not visible. The interactions of the internal and external flows affect the drag of the nozzle. Because the displacement of the external flow at the lower nozzle pressure ratios is smaller, the drag caused by the external shocks (Fig. 11) is therefore also smaller.

The influence of the freestream Reynolds number was also investigated, but, as Figs. 20a and 20b show, the influence is rather small (if, indeed, not negligible) in the investigated region. Noticeable differences can only be found at the very bottom and at the top right-hand corner. This may be partially due to the fact that the

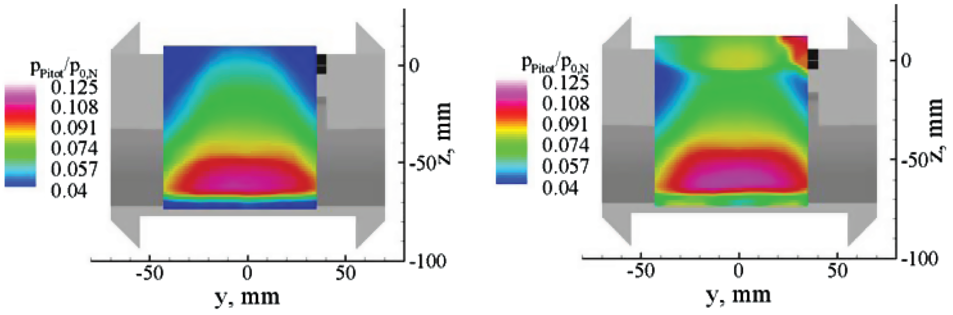

a) $\Pi = 500$ and $Re_U = 8.10^6$ $x = 220$ mm

b) $\Pi = 250$ and $Re_U = 8.10^6$ $x = 220$ mm

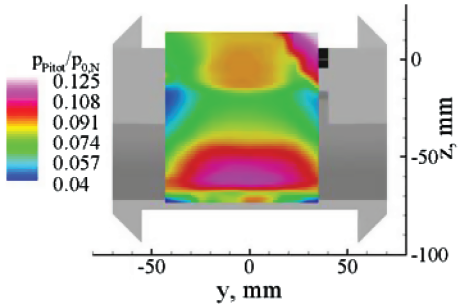

c) $\Pi = 191$ and $Re_U = 8.10^6$ $x = 220$ mm

Fig. 19 Pitot pressure measurements for different nozzle pressure ratios Π ($Re_U = 8 \times 10^6$ and downstream position $x = 220$ mm are the same for all three figures).

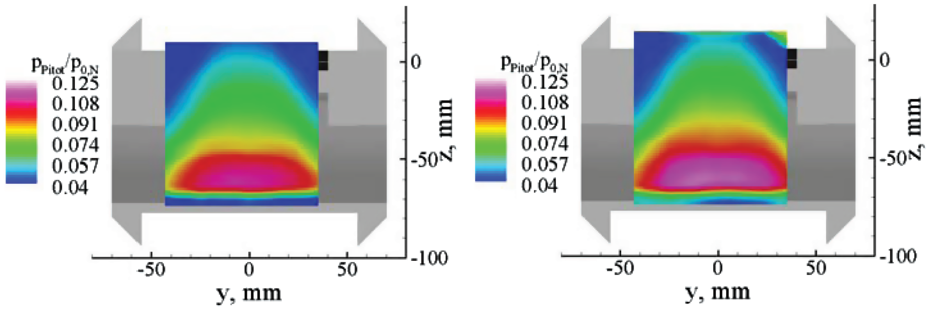

a) $\Pi = 500$ and $Re_U = 8.10^6$ $x = 220$ mm

b) $\Pi = 500$ and $Re_U = 4.10^6$ $x = 220$ mm

Fig. 20 Pitot pressure measurements for different freestream Reynolds numbers ($\Pi = 500$ and downstream position $x = 220$ mm are the same for both figures).

nozzle pressure ratio is not exactly $\Pi = 500$ in both cases, so that the observed differences may be a nozzle pressure ratio rather than a Reynolds number effect. It is very difficult with this wind tunnel to match the conditions from one run to the next exactly, so that small variations in Π are always possible.

B. Thrust of the Single Expansion Ramp Nozzle

1. *Ideal Thrust*

The ideal thrust F_{id} is needed to calculate the thrust efficiency and to estimate the performance of the nozzle. The governing equation (1) for the ideal thrust can be expressed in the following way (ρ_A, V_A, and A_A are the density, velocity, and area at the nozzle exit plane, respectively):

$$\begin{aligned} F_{\text{id}} &= \rho_A \cdot V_A^2 \cdot A_A = \rho_A \cdot V_A^2 \cdot A_E \cdot \frac{A_A}{A_E} \\ &= \frac{p_A}{R \cdot T_A} \cdot Ma_A^2 \cdot \gamma \cdot R \cdot T_A \cdot A_E \cdot \frac{A^*}{A_E}\frac{A_A}{A^*} \\ &= A_E \cdot \frac{A^*}{A_E} \cdot p_A \cdot \gamma \cdot Ma_A^2 \cdot \frac{A_A}{A^*} \end{aligned} \tag{1}$$

With $p_A = p_\infty$ and $p_{0,N}$ as the nozzle total pressure, the equation for the ideal thrust becomes

$$F_{\text{id}} = A_E \cdot \frac{A^*}{A_E} \cdot p_{0,N} \cdot \frac{p_\infty}{p_{0,N}} \cdot \gamma \cdot Ma_A^2 \cdot \frac{A_A}{A^*} \tag{2}$$

By inserting the following relations:

$$\begin{aligned} \frac{p_\infty}{p_{0,N}} &= \left(1 + \frac{(\gamma - 1)}{2} \cdot Ma_A^2\right)^{\frac{\gamma}{\gamma-1}} \\ \Rightarrow Ma_A^2 &= \left[\left(\frac{p_{0,N}}{p_\infty}\right)^{\frac{\gamma-1}{\gamma}} - 1\right] \cdot \frac{2}{\gamma - 1} \end{aligned}$$

and

$$\frac{A_E}{A^*} = \frac{\left[\frac{2}{\gamma+1} \cdot \left(1 + \frac{\gamma-1}{2} Ma_E^2\right)\right]^{\frac{\gamma+1}{2(\gamma-1)}}}{Ma_E}$$

into Eq. (2), the final equation for the ideal thrust then becomes

$$F_{\mathrm{id}} = A_E \cdot p_{0,N} \cdot \sqrt{\frac{2 \cdot \gamma^2}{\gamma - 1} \cdot \left(\frac{2}{\gamma + 1}\right)^{\frac{\gamma+1}{\gamma-1}} \cdot (1 - \Pi^{\frac{1-\gamma}{\gamma}})} \cdot \frac{Ma_E}{[\frac{2}{\gamma+1} \cdot (1 + \frac{\gamma-1}{2} Ma_E^2)]^{\frac{\gamma+1}{2(\gamma-1)}}} \tag{3}$$

This is the maximum gross thrust that an optimized nozzle could generate, neglecting drag and other losses. The ideal thrust can only be obtained with a parallel flow at the end of nozzle. In reality, however, to meet this criterion would result in an oversized nozzle, increasing its weight and drag considerably. Because most of the thrust is generated at the beginning of the nozzle, the benefit in thrust of a longer nozzle is not compensated by the increase in weight and drag of such long nozzles [30,31]. Therefore the nozzles of scramjet engines are truncated at a certain position and integrated into the airframe to reduce their overall size and weight [12,32]. The Rao criterion [33] is used to truncate the nozzle and to design its contour so that the maximum thrust is obtained with the given truncation.

The truncation of the nozzle causes a lower thrust than ideally possible; hence the thrust efficiency coefficient c_{fg} is introduced in Eq. (4) to measure the deviation from the ideal thrust and to quantify the performance of a nozzle:

$$c_{\mathrm{fg}} = \frac{F}{F_{\mathrm{id}}} \tag{4}$$

Another important indication of the performance of the nozzle is the thrust vector angle β_f [Eq. (5)], defined as

$$\beta_f = \arctan \frac{F_z}{F_x} \tag{5}$$

Depending on the size of the thrust vector angle, the flight vehicle may have to be trimmed to guarantee a stable flight path. The higher the thrust vector angle, of course, the greater the efforts needed to trim the flight vehicle. These then are the three factors needed to assess the performance of a nozzle and to compare its performance with other configurations and other nozzles: the gross thrust F, the thrust efficiency coefficient c_{fg}, and thrust vector angle β_f.

Figure 21 shows the ideal thrust as a function of the nozzle pressure ratio for a nozzle total pressure of $p_{0,N} = 1.33$ bar and a Mach number at the entrance of the nozzle of $Ma_E = 2$. It can be seen that the ideal thrust increases with increasing nozzle pressure ratio, but that the growth rate also decreases, with the value for F_{id} approaching a value of about 2285 N asymptotically (for the present nozzle total pressure $p_{0,N}$, Mach number Ma_E, and entrance area A_E of the nozzle). The ideal thrust can be increased by a higher nozzle total pressure $p_{0,N}$, a higher entrance area A_E, or a smaller entrance Mach number Ma_E. The aim of the combustion process is to obtain high nozzle total pressures and lower Mach numbers at the end of the combustion chamber and beginning of the nozzle to obtain high ideal thrusts. With increasing nozzle total pressures, the nozzle pressure ratio also increases as long as the freestream pressure is constant, that is, as long as the flight path altitude of the flight vehicle does not change markedly.

2. *Measured Generated Thrust*

The thrust that is actually generated by the designed nozzle is calculated in two ways in the present work to highlight the differences and the influence of the 3-D expansion of the nozzle flow on the thrust: thrust is calculated from pressure data measured by the PSI pressure transducers (embedded sensors) and also by the PSP technique. Because of geometrical restrictions in the experimental setup and the resulting impeded optical access, the PSP pressure data could only be obtained at streamwise x positions from $x = 20$ mm until the end of the expansion ramp at $x = 200$ mm. Hence the region in which PSP results are available, see the measurement zone of influence indicated by the dashed rectangle in Fig. 22, does not cover the whole surface of the ramp. The pressure data are available at any grid point inside this rectangle, where grid distances of $\Delta x = 1$ mm and $\Delta y = 1$ mm apply. With the PSP technique the pressure data of this entire surface are obtained, whereas with the PSI pressure transducers the pressure is obtained only at discrete locations (black dots in Fig. 22).

Equations (6–12) used to calculate the forces from the pressure data obtained by the PSP technique are

$$\mathrm{d}F_x = (p_{i,j} - p_\infty) \cdot \Delta l_{i,j} \cdot \Delta y_{i,j} \cdot \sin \beta_{i,j} \tag{6}$$

$$\mathrm{d}F_z = (p_{i,j} - p_\infty) \cdot \Delta l_{i,j} \cdot \Delta y_{i,j} \cdot \cos \beta_{i,j} \tag{7}$$

$$\Delta l_{i,j} = \sqrt{\Delta x_{i,j}^2 + \Delta z_{i,j}^2} \tag{8}$$

$$\beta_{i,j} = \arctan\left(\frac{\Delta z_{i,j}}{\Delta x_{i,j}}\right) \tag{9}$$

$$\Delta x_{i,j} = \frac{x_{i,j+1} - x_{i,j-1}}{2} \tag{10}$$

$$\Delta y_{i,j} = \frac{y_{i+1,j} - y_{i-1,j}}{2} \tag{11}$$

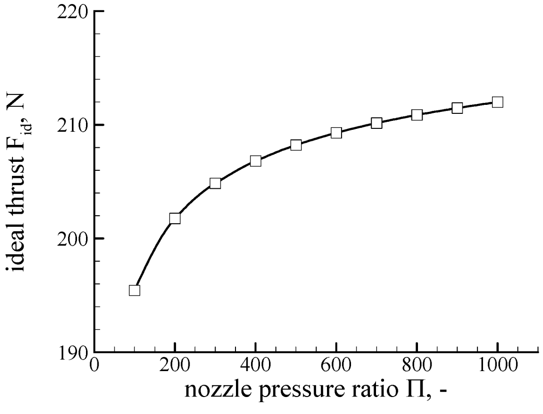

Fig. 21 Ideal thrust for air and a nozzle total pressure of $p_{0,N} = 1.33$ bar.

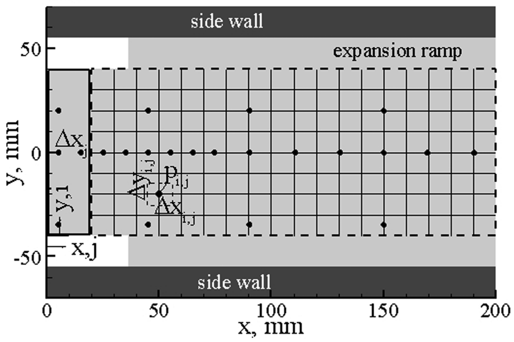

Fig. 22 Measurement zone of influence of PSP and PSI as well as the grid used here for calculation of thrust from the PSI and PSP pressure measurements (see text).

$$\Delta z_{i,j} = \frac{z_{i,j+1} - z_{i,j-1}}{2} \tag{12}$$

To obtain the forces on the entire surface where the PSP technique was applied, the forces at every single grid point have to be added according to the following Eqs. (13–15):

$$F_x(\mathrm{PSP}) = \sum \mathrm{d}F_{xi,j} \tag{13}$$

$$F_z(\mathrm{PSP}) = \sum \mathrm{d}F_{z_{i,j}} \tag{14}$$

$$F_{\mathrm{tot}}(\mathrm{PSP}) = \sqrt{F_x^2 + F_z^2} \tag{15}$$

The equations used to calculate the forces with the pressure data obtained by the PSI transducers look similar to the ones for the PSP technique, but the indices differ. The reason for that is that with the data from the PSI transducers only a 2-D force can be calculated along the line of the pressure transducers. The 3-D force is then computed by multiplying with the width of the corresponding measurement zone, leading thus to the Eqs. (16–21) to be used here

$$\mathrm{d}F_x = (p_j - p_\infty) \cdot \Delta l_j \cdot \sin \beta_j \tag{16}$$

$$\mathrm{d}F_z = (p_j - p_\infty) \cdot \Delta l_j \cdot \cos \beta_j \tag{17}$$

$$\Delta l_j = \sqrt{\Delta x_j^2 + \Delta z_j^2} \tag{18}$$

$$\beta_j = \arctan\left(\frac{\Delta z_j}{\Delta x_j}\right) \tag{19}$$

$$\Delta x_j = \frac{x_{j+1} - x_{j-1}}{2} \tag{20}$$

$$\Delta z_j = \frac{z_{j+1} - z_{j-1}}{2} \tag{21}$$

Now the forces at the single PSI transducers have to be summed to obtain the 2-D force along the entire line leading to the following Eqs. (22–24):

$$F_x(\mathrm{PSI}) = \sum \mathrm{d}F_{x_j} \tag{22}$$

$$F_z(\mathrm{PSI}) = \sum \mathrm{d}F_{z_j} \tag{23}$$

$$F_{\mathrm{tot}}(\mathrm{PSI}) = \sqrt{F_x^2 + F_z^2} \quad \text{(2-D force)} \tag{24}$$

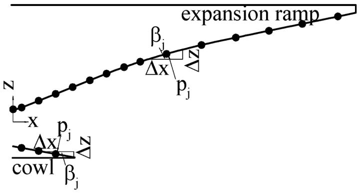

Fig. 23 Spline interpolation for PSI pressure transducers.

Two different methods for calculating the thrust over the whole ramp surface from the PSI pressure measurements will be discussed.

Method 1: Here the thrust obtained via the pressures from the PSI transducers and via the PSP technique inside the dashed rectangle is calculated, whereby only the PSI pressure transducers along the centerline are used. To compute the thrust with the PSI pressure data at points where there are no sensors, it is assumed that the pressure is constant between two single pressure orifices in a streamwise (x) direction. First, the thrust is calculated along the line where the pressure orifices are to be found. This is done with a spline interpolation, as shown in Fig. 23.

Secondly, the thrust of the entire expansion ramp is calculated by multiplying the thrust along the centerline with the corresponding width of the dashed rectangle, that is, 80 mm. Obviously, there must be large differences between the thrust calculated using the PSI pressure data in this way and that calculated using the PSP pressure data, because the pressure is clearly not constant over the total y direction, due to the 3-D expansion of the nozzle flow. The comparison of the thrust determined from PSI and PSP data is shown in Table 2. Here it can be seen that the difference in calculated thrust from the two measurement techniques, for both F_x and F_z, lies between 20 and 30%. The table shows that the forces in the x and the z directions are higher when calculated from the PSI pressure data. This makes sense, due to the fact that in this case the expansion of the flow in the y direction, with its concomitant pressure and hence thrust decrease, is not taken into account. Because the flow closer to the side walls, however, has a lower pressure than along the centerline, the thrust calculated by only the PSI pressure data must be too high. This comparison also reveals the large error introduced by attempting to obtain meaningful thrust data from pressure measurements at discrete points along a single line only for the cases where there are pressure gradients over the surface.

Method 2: As a further development of the simplification adopted in method 1, the other two lines of pressure transducers to the left ($y = 20$ mm) and right sides ($y = -35$ mm) of the centerline are now also included in the calculation of thrust from the PSI pressure data. Because the PSP pressure measurements showed that the nozzle flow is largely symmetrical about the centerline $y = 0$, in this method the pressure values are mirrored about this centerline to obtain the pressure data at the opposing y locations, that is, $y = -20$ mm and $y = 35$ mm; this leads to five so-called zones of influence of the PSI transducers for this second comparison, as shown in Fig. 24.

Again the thrusts obtained from the two different (PSI and PSP) techniques are calculated and compared as follows: $p_{0,N} = 0.98$ bar, $T_{0,N} = 279.51$ K, $\Pi = 383.62$, $F_{x,\mathrm{PSP}} = 6.43$ N, $F_{z,\mathrm{PSP}} = 22.07$ N, $F_{x,\mathrm{PSI}} = 6.73$ N, $F_{z,\mathrm{PSI}} = 23.64$ N, $\Delta F_x = 5.0\%$, and $\Delta F_z = 7.0\%$. In this case the differences are lower than in the first case, but still there is a marked difference between the two thrusts. The forces in the x and the z directions derived from the PSI pressure measurements are also higher here, as with method 1, only this time the differences between the forces are around 5% for the thrust (x) force and 7% for

Table 2 Derivation of thrust calculated by PSI (along the centerline) and PSP pressure measurements

$p_{0,N}$, bar	$T_{0,N}$, K	Π	$F_{x,\mathrm{PSP}}$, N	$F_{x,\mathrm{PSI}}$, N	ΔF_x, %	$F_{z,\mathrm{PSP}}$, N	$F_{z,\mathrm{PSI}}$, N	ΔF_z, %
0.98	279.5	384	6.4	8.0	24.0	22.1	28.7	30.0
2.03	284.1	435	13.2	16.0	22.0	44.9	57.4	28.0

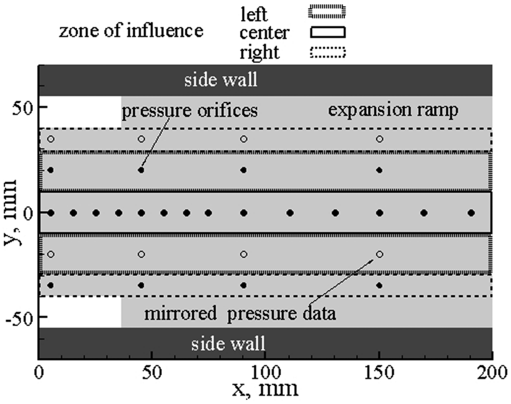

Fig. 24 Zones of influence of PSI pressure transducers for calculating the thrust of the nozzle.

the lift (z) force. The reason for this discrepancy is again that the pressure in the far outside regions of the expansion ramp is not accurately known with the PSI pressure transducers, so that the simplification with the zones of influence used here leads again to an overestimation of the pressure values at these side regions.

Because of the fact that the nozzle net thrust is very sensitive to any disturbances and losses in the combustion chamber [1], it is mandatory to be able to predict the available thrust as accurately as possible. Because a nozzle has to generate a positive net thrust to accelerate the vehicle, and because this net thrust is the difference between the total thrust and the total drag, both quite large values, the predictions must be known to quite a considerable degree of accuracy. An improper estimation of the generated thrust can lead to a catastrophic flight failure. The measurements shown here demonstrate very nicely the necessity and the advantage of the PSP technique in obtaining meaningful thrusts with sufficient accuracy and over the whole surface of a thrust ramp.

After having compared the two different methods of calculating the thrust in the dashed rectangular zone of influence (see Figs. 22 and 24), now the thrust for the entire nozzle surface is calculated. This is done by using the available PSP pressure data inside the rectangular zone, and the PSI pressure data on the ramp inside the black rectangular zone ($x < 20$ mm, Fig. 22), and also on the cowl. The following equations are applied:

$$F = \rho \cdot V^2 \cdot A + F_{\mathrm{tot}}(\mathrm{PSP}) + F_{\mathrm{tot}}(\mathrm{PSI}, x < 20\ \mathrm{mm}) \tag{25}$$

$$\begin{aligned} F = {} & \rho \cdot V^2 \cdot h \cdot 0.08 + F_{\mathrm{tot}}(\mathrm{PSP}) + F_{\mathrm{tot}}(\mathrm{center}, x < 20\ \mathrm{mm}) \cdot 0.02 \\ & + 2 \cdot [F_{\mathrm{tot}}(\mathrm{left}, x < 20\ \mathrm{mm}) \cdot 0.0125 \\ & + F_{\mathrm{tot}}(\mathrm{right}, x < 20\ \mathrm{mm}) \cdot 0.0175] \end{aligned} \tag{26}$$

The total force F consists of three components [Eq. (25)]: the momentum part, the contribution of the force obtained from PSP, and the contribution of the force from PSI measurements. The PSI force is further divided into five parts, where the centerline determines a zone of influence of width 20 mm, the left line a zone of 12.5 mm width, and the right line a zone of 17.5 mm width, the sum in width of all zones accounting for the total width of the ramp (80 mm). On the cowl there are only three pressure transducers, so that a spline interpolation along the centerline of the cowl is used. The thrust along this line is then multiplied by the width of the cowl, leading to the total force generated on the cowl. The entire thrust is then computed by using Eqs. (25) and (26), where the contribution of the momentum at the entrance of the nozzle is also included. The governing equation to calculate the thrust generated by the nozzle is as follows, taking into account the momentum and pressure along the wall surfaces [34]:

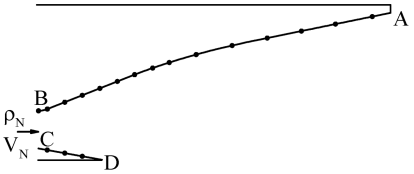

Fig. 25 Integration boundaries for thrust calculation with positions of PSI pressure transducer taps.

$$\mathbf{F} = -b \cdot \left[\int_A^D (p - p_\infty) \cdot \mathbf{n} \cdot \mathrm{d}s + \int_B^C \rho \cdot \mathbf{V} \cdot (\mathbf{V} \cdot \mathbf{n}) \mathrm{d}s \right] \tag{27}$$

The integration boundaries for the thrust calculation and the position of the pressure transducers along the centerline of the expansion ramp and the cowl are shown in Fig. 25.

The thrust is calculated for different combinations of wind-tunnel run parameters to study the effects of the nozzle pressure ratio and freestream Reynolds number on the thrust. The results for this parameter variation are shown in Table 3, where the total thrust, the forces in the x and z directions, the total thrust efficiency coefficient, the thrust efficiency coefficient in the x direction, and the thrust vector angle are listed as a function of the nozzle total pressure $p_{0,N}$ and nozzle pressure ratio Π. The table shows that the thrust increases with both the nozzle total pressure and the nozzle pressure ratio.

3. *Thrust Losses*

To estimate the thrust losses, the calculated (from pressure measurements) 3-D thrust without side walls and the possible 2-D thrust with sidewalls are compared. These losses are mainly due to the flush-mounted side walls, which lead to an expansion of flow in the y direction and thus to pressure and hence thrust losses. The 2-D thrust is calculated by taking the thrust along the centerline into account and multiplying it by the width of the single expansion ramp, applying the assumption that the force is constant over the width (in the y direction). The results in Table 4 show the differences between the two thrusts $F_{2\text{-D}}$ and $F_{3\text{-D}}$ for different nozzle total pressures and

Table 3 Derivation of thrust calculated from PSI (along the center, right, and left lines) and PSP pressure measurements

$p_{0,N}$	Π	$F_{x,\mathrm{tot}}$	$F_{z,\mathrm{tot}}$	F_{tot}	$c_{\mathrm{fg,tot}}$	$c_{\mathrm{fg},x}$	β_f
0.51	214	84.9	6.6	85.1	0.961	0.958	4.44
1.38	291	199.9	14.7	200.4	0.945	0.942	4.20
2.03	435	295.4	23.9	296.3	0.937	0.934	4.63
1.26	512	183.7	15.1	184.3	0.934	0.931	4.71
1.34	531	195.6	16.4	196.3	0.933	0.930	4.79
2.62	568	382.5	31.7	383.8	0.932	0.928	4.73
2.53	981	369.4	32.2	370.8	0.921	0.918	4.98
2.57	1038	375.4	32.5	376.8	0.920	0.916	4.95

Table 4 Differences in the forces calculated for the 2-D and 3-D cases for different nozzle total pressures and nozzle pressure ratios

$p_{0,D}$, bar	Π	F_{2D}, N	$F_{3\text{-D}}$, N	ΔF, %
0.47	180	67.78	66.96	1.22
0.95	202	139.51	137.60	1.39
0.51	214	86.17	85.14	1.21
0.42	257	61.57	60.90	1.10
1.38	291	202.53	200.42	1.05
0.98	384	145.13	143.77	0.95
2.03	435	298.81	296.34	0.83
0.82	505	121.2	120.15	0.87
1.26	512	185.95	184.30	0.90
1.34	531	198.09	196.33	0.90
2.62	568	386.89	383.84	0.79
1.64	654	242.56	240.80	0.73
2.53	981	373.47	370.81	0.72
2.57	1038	379.35	376.78	0.68

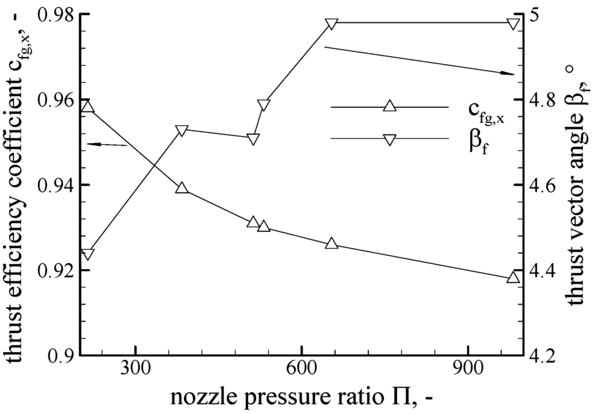

Fig. 26 Thrust efficient coefficient and thrust vector angle for different nozzle pressure ratios.

nozzle pressure ratios. It can be seen that these differences lie between 0.68 and 1.38%, which is quite low, but nevertheless still significant. The reason for these differences is again that some components of the 3-D thrust must be calculated using the PSI pressure data, because the PSP pressure data were not available on the entire nozzle surface. Another reason for the fairly small differences is that the momentum component at the entrance of the nozzle [see Eq. (25)] supplies the major contribution to the thrust, and this is of course the same for the 2-D and the 3-D cases.

The flush-mounted side walls do not only cause thrust losses, but also lead to a reduction of the structural weight and a lessening of the drag forces due to friction. It is therefore necessary to evaluate which one of the two effects is stronger, the thrust losses or the drag losses. The structural weight can be easily calculated and depends mainly on the material used. To estimate the drag due to friction, further experiments and/or numerical calculations are required. If both weight and drag are known, the influence of the side walls on the net thrust can be estimated. This estimation is an important contribution to the design process of the nozzle, providing an answer to the question of whether the side walls are beneficial or deleterious.

In Fig. 26 the thrust efficiency coefficient and the thrust vector angle [35] are plotted as a function of the nozzle pressure ratio Π. The results show that the higher the nozzle pressure ratio, the lower the thrust efficiency, the thrust efficiency coefficient having a maximum value of 95.8% at $\Pi = 214$, and falling to only 91.6% at $\Pi = 1038$. For a constant freestream Reynolds number, a higher nozzle pressure ratio implies a higher nozzle total pressure and hence a higher thrust. A glance at Table 4 shows that the highest thrust $F = 383.8$ N is obtained for the highest nozzle total pressure $p_{0,N} = 2.62$ bar with a corresponding nozzle pressure ratio of $\Pi = 568$ (this is, however, not the maximum value of Π), and the lowest thrust $F = 85.1$ N is obtained for the lowest nozzle total pressure $p_{0,N} = 0.51$ bar with a corresponding nozzle pressure ratio $\Pi = 214$.

Higher nozzle total pressures produce higher thrusts, but at the same time the exhaust plume enlarges with higher nozzle pressure ratios, which also leads to higher base drags. The shocks which are generated from the displacement of the outer flow are more oblique at higher nozzle pressure ratios due to the stronger displacement of the outer flow. This therefore places a limit on how much the nozzle pressure ratio can be increased. An iterative approach is needed to find an optimal compromise between maximizing the generated thrust while minimizing the ensuing drag caused by the exhaust plume. The thrust vector angle β_f, however, must also be considered; because the vehicle has to be trimmed to maintain the flight path, larger values of β lead to more required effort to control the vehicle. In Fig. 26 β_f is shown to be strongly dependent on the nozzle pressure ratio, its value increasing for higher Π. This exemplifies another disadvantage of using higher nozzle pressure ratios; the flight vehicle has to be trimmed more excessively for higher thrust vector angles than for lower angles. The thrust vector angle varies between 4.2 and 5.0 deg, a change of about 16%, which is certainly not negligible. It is therefore important to not only focus on the gross thrust, but also on the thrust efficiency, the drag that is caused by the exhaust plume, and the thrust vector angle in order to be able to find the optimal conditions for the scramjet nozzle. This leads to the conclusion that high nozzle total pressures with low nozzle pressure ratios have to be obtained to generate high thrust, whereas the thrust vector angle should be close to zero to avoid the need of excessive trimming.

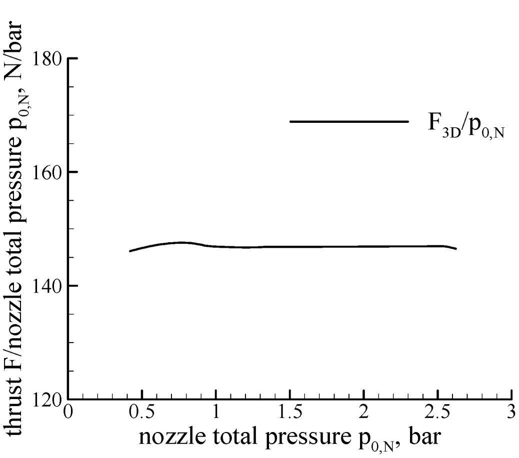

Fig. 27 Thrust of the nozzle divided by the nozzle total pressure for different nozzle total pressures.

Another interesting observation for this nozzle type within the investigated region of nozzle pressure ratio and freestream Reynolds number is revealed in Fig. 27. Here the thrust F normalized to the nozzle pressure ratio $p_{0,N}$ is plotted against the nozzle total pressure $p_{0,N}$. As can be seen, the plot is nearly constant over the investigated region of $p_{0,N}$, its highest and lowest values lying at 147.5 and 145 N/bar, respectively, which corresponds to a maximum variation of only 1.6%. This result, the constancy of this normalized value versus $p_{0,N}$, enables one to estimate the thrust for this particular nozzle type very accurately for all values of $p_{0,N}$ between 0.51 and 2.62 bar. The nozzle total pressure has just to be multiplied by the constant value obtained from the graph to yield the thrust of the nozzle. To generalize this statement for other nozzles a broader experimental study with different nozzle contours would of course have to be performed. For the present nozzle, however, the approach applies and provides a quick aid in computing the thrust for any condition without having to carry out the experiment.

Based on these observations, a new coefficient $F/p_{0,N}$ could be introduced as an aid in judging the performance of single expansion ramp nozzles. If the above assumption can be generalized for asymmetric nozzles, this coefficient can be easily calculated and used for any nozzle. Therefore, the goal should be to design a nozzle with a very high value of this coefficient: the higher this coefficient is, the more thrust is generated.

IV. Conclusions

An experimental study has been conducted with a nozzle/afterbody model to characterize the flowfield created by the interaction of a single expansion ramp nozzle flow with an external hypersonic flow. For a better understanding of the physical phenomena involved, of the influence of different parameters on the nozzle flow properties and nozzle performance, as well as of the complex interactions between the internal nozzle and the external flows, the pitot pressure measurement and the PSP methods have been applied. Both methods were also used to calculate the nozzle thrust, with different assumptions being made on how to process and combine the PSI and PSP pressure data.

The PSP results showed the normalized pressure distribution on the expansion ramp to be independent of the nozzle pressure ratio and the freestream Reynolds number in the investigated region. The pressure distribution on the surface of the expansion ramp was obtained and compared for different nozzle pressure ratios and freestream Reynolds number. The main influence on the gross thrust was seen to be the nozzle pressure ratio and the nozzle total pressure.

The pitot pressure measurements, however, revealed a strong influence of the nozzle pressure ratio on the flowfield in the wake of the nozzle, due to the different size of the exhaust plume for different nozzle pressure ratios. The size of the exhaust plume affects the interactions between the internal nozzle flow and the external flow, leading to different flow patterns in the measured plane in the wake of the nozzle. The main supersonic core nozzle flow is not influenced by the external flow conditions (i.e., neither by Π nor by Re_U), whereas the behavior of the shear layer has been shown to be influenced by these two flow condition parameters.

The gross thrust, thrust efficiency coefficient, and thrust vector angle were calculated from the PSI and PSP pressure results and compared for different nozzle pressure ratios. The results show that the gross thrust increases with growing nozzle pressure ratio for a constant freestream Reynolds number, while the thrust efficiency coefficient decreases with growing nozzle pressure ratio and the thrust vector angle increases. Because the goal of the nozzle design process is high thrust and low thrust vector angles, a compromise in the value of the nozzle pressure ratio has to be made. Higher nozzle pressure ratios also cause a stronger displacement of the external flow, enlarging the drag due to pressure losses over the oblique shocks. It can also be said that the gross thrust depends mainly on Π, but does not depend strongly on Re_U, at least not within the investigated Reynolds number range here. The total net thrust of the scramjet engine, however, obviously depends on the freestream Reynolds number.

The forces calculated from pressure measurements from the PSI transducers and from the PSP technique were compared in the region where the PSP paint was applied. It was found that the differences in calculated thrust from these two methods can be as high as 30% if only the PSI pressure values along the centerline are used to calculate the forces. If the other lines of PSI sensors (left and right) are also included in the calculation, then the differences decrease to about 7%, which, however, still represents a marked difference. Therefore, the PSP technique allows a more accurate calculation of the pressure forces on the expansion ramp, because it provides a detailed, spatially resolved pressure distribution over the entire ramp surface. Because the thrust of a scramjet nozzle is very sensitive to parameter changes in the intake and combustion chamber and must be known very precisely for the design of the vehicle, an accurate knowledge of the thrust becomes mandatory.

Acknowledgments

The financial support for this work by the German National Research Council (DFG) within the Graduate Student Research Group “Aerothermodynamic Design of a Scramjet Propulsion System for Future Space Transportation” and by the German Aerospace Center (DLR) is gratefully acknowledged. The authors would especially like to thank the following colleagues at the Institute of Aerodynamics and Flow Technology for their valuable contributions to this work: Ch. Klein, W. Sachs, U. Fey, P. Gruhn, J. Häberle, P. Herzog, M. Janke, and D. Lütz.

References

[1] Walther, R., “Scramjet-Propulsion: alte Herausforderung im neuen Jahrhundert?” *Jahrbuch 2003 der Deutschen Gesellschaft für Luft- und Raumfahrt—Lilientahl-Obert*, DGLR, Munich, 2003, pp. 755–764.

[2] Curran, E. T., and Murthy, S. N. B., *Scramjet Propulsion*, Vol. 189, AIAA, Reston, VA, 2000.

[3] Fry, R. S., “A Century of Ramjet Propulsion Technology Evolution,” *Journal of Propulsion and Power*, Vol. 20, No. 1, 2004, pp. 27–58. doi:10.2514/1.9178

[4] Spaid, F. W., and Keener, E. R., “Hypersonic Nozzle/Afterbody CFD Code Validation Part 1: Experimental Measurements,” AIAA 93-0607, 1993.

[5] Spaid, F. W., Keener, E. R., and Hui, F. C. L., “Experimental Results for a Hypersonic Nozzle/Afterbody Flow Field,” NASA Ames Research Center, NASA TM-4638, 1995.

[6] Gruhn, P., Henckels, A., and Sieberger, G., “Improvement of the SERN Nozzle Performance by Aerodynamic Flap Design,” *Aerospace Science and Technology*, Vol. 6, No. 6, 2002, pp. 395–405. doi:10.1016/S1270-9638(02)01177-X

[7] Flandro, G. A., Roach, R. L., and Buschek, H., “Dynamic Interactions Between Hypersonic Vehicle Aerodynamics and Propulsion System Performance,” NASA Center for AeroSpace Information (CASI), NASA CR-190638, 1992.

[8] Edwards, T. A., “The Effect of Exhaust Plume/Afterbody Interaction on Installed Scramjet Performance,” NASA Center for AeroSpace Information (CASI), NASA TM-101033, 1988.

[9] Baysal, O., “Flow Analysis and Design Optimization Methods for Nozzle Afterbody of a Hypersonic Vehicle,” NASA Center for AeroSpace Information (CASI), NASA CR-4431, 1991.

[10] Ebrahimi, H. B., “An Efficient Two-Dimensional Engineering Design Code for Scramjet Combustor, Nozzle, and Plume Analysis,” AIAA 91-0416, 1991.

[11] Ishiguro, T., Takaki, R., Mitani, T., and Hiraiwa, T., “Three-Dimensional Analysis of Scramjet Nozzle Flows,” *AIAA/DGLR Fifth International Aerospace Planes and Hypersonics Technologies Conference*, AIAA, Washington, D.C., 1993.

[12] Tatum, K., Monta, W., Witte, D., and Walters, R., “Analysis of Generic Scramjet External Nozzle Flowfields Employing Simulant Gases,” AIAA 90-5242, 1990.

[13] Keener, E. R., “Experimental Research of the Aerodynamics of Nozzles and Plumes at Hypersonic Speeds,” NASA Center for AeroSpace Information (CASI), NASA CR-187316, 1992.

[14] Carboni, J. D., Shyne, R. J., Leavitt, L. D., Taylor, J. G., and Lamb, M., “Supersonic Investigation of Two Dimensional Hypersonic Exhaust Nozzles,” NASA Center for AeroSpace Information (CASI), NASA TM-105687, 1992.

[15] Lindblad, I. A. A., Grönland, T. A., Cambier, J.-L., Wallin, S., Behrens, T. M., Sacher, P., and Netterfield, M., “A Study of Hypersonic Afterbody Flowfields,” AIAA 97-2289, 1997.

[16] Tomioka, S., Hiraiwa, T., and Mitani, T., “A Study on Boundary Layer in a Scramjet Nozzle Operating Under High Enthalpy Conditions,” *30th AIAA/ASME/SAE/ASEE Joint Propulsion Conference*, AIAA, Washington, D.C., 1994.

[17] Weigand, B., Gaisbauer, U., Reinhartz, B., Kau, H.-P., and Schröder, W., “Aero-Thermodynamische Auslegung eines Scramjets—Antriebssystems für Zukünftige Raumtransportsysteme,” *DGLR-Tagung*, 2006.

[18] Mitani, T., Kanda, T., Hiraiwa, T., Igarashi, Y., and Nakahashi, K., “Drags in Scramjet Engine Testing: Experimental and Computational Fluid Dynamics Studies,” *Journal of Propulsion and Power*, Vol. 15, No. 4, 1999, pp. 578–583. doi:10.2514/2.5466

[19] Hirschen, C., Gülhan, A., Beck, W. H., and Henne, U., “Experimental Study of a Scramjet Nozzle Flow Using the Pressure Sensitive Paint Method,” *Journal of Propulsion and Power*, Vol. 24, No. 4, 2008, pp. 662–672. doi:10.2514/1.34626

[20] Zucrow, M. J., and Hoffman, J. D., *Gas Dynamics Volume 2 Multidimensional Flow*, Krieger, Malabar, FL, 1985.

[21] Hubner, J. P., Carroll, B. F., Schanze, K. S., Ji, H. F., and Holden, M. S., “Temperature- and Pressure-Sensitive Paint Measurements in Short-Duration Hypersonic Flow,” *AIAA Journal*, Vol. 39, No. 4, 2001, pp. 654–659. doi:10.2514/2.1358

[22] Matsumura, S., Schneider, S. P., and Berry, S. A., “Streamwise Vortex Instability and Transition on the Hyper-2000 Scramjet Forbeody,” *Journal of Spacecraft and Rockets*, Vol. 42, No. 1, 2005, pp. 78–89. doi:10.2514/1.3959

[23] U. Gaisbauer, B. W., Reinartz, B., Kau, H. P., and Schröder, W., “Research Training Group GRK 1095/1: “Aero-Thermodynamic Design of a Scramjet Propulsion System”,” *8th International Symposium on Air Breathing Engines*, AIAA, Reston, VA, 2007.

[24] Hirschen, C., Gruhn, P., and Gülhan, A., “Influence of Heat Capacity Ratio on the Interaction Between External Flow and Nozzle Flow of a Scramjet,” AIAA 2006-8095, 2006.

[25] Hirschen, C., Gülhan, A., Beck, W. H., and Henne, U., “Experimental Study of the Interaction Between Internal and External Flows of a Scramjet Nozzle Using Various Diagnostic Techniques,” AIAA 2007-5088, 2007.

[26] Hirschen, C., and Gülhan, A., “Experimental Study of the Single Expansion Ramp Nozzle Flow Properties and its Interaction with the External Flow,” *1st CEAS European Air and Space Conference*, DGLR, Berlin, 367, 2007.

[27] Niezgodka, F.-J., “Der Hyperschallwindkanal H2K des DLR in Köln Porz (Stand 2000),” DLR Report, ISSN 1434-8462, 2001.

[28] Klein, C., Niebergall, S., Sachs, W. E., Henne, U., and Engler, R. H., "PSP Measurements on a Linear Plug Nozzle: Aerodynamic Investigation of Linear Plug Nozzle Configurations," *New Results in Numerical and Experimental Fluid Mechanics IV, Notes on Numerical Fluid Mechanics and Multidisciplinary Design (NNFM)*, edited by C. Breitsamter, B. Laschka, H.-J. Heinemann, and R. Hilbig, Vol. 87, Springer, New York, 2004, pp. 260–269.

[29] Henckels, A., Gülhan, A., and Neeb, D., "An Experimental Study on the Base Flow Plume Interaction of Booster Configurations," *1st CEAS Europen Air and Space Conference*, DGLR, Berlin, 29, 2007.

[30] Perrier, P., Rapuc, M., Rostand, P., Hallard, R., Regard, D., Dufour, A., and Penanhoat, O., "Nozzle and Afterbody Design for Hypersonic Airbreathing Vehicles," AIAA Paper 96-4548, 1996.

[31] Shyne, R. J., and Keith, T. G., "Analysis and Design of Optimized Truncated Scarfed Nozzles Subject to External Flow Effects," NASA Center for AeroSpace Information (CASI), NASA TM-103175, 1990.

[32] Hollmeier, S., Esch, T., Herrmann, O., and Rick, H., "Propulsion/Aircraft Integration and Dynamic Performance of Hypersonic TSTO Vehicles," *12th International Symposium on Airbreathing Engines*, AIAA, Washington, D.C., 1995.

[33] Rao, G. V. R., "Exhaust Nozzle Contour for Optimum Thrust," *Jet Propulsion*, Vol. 28, No. 6, 1958, pp. 377–382.

[34] Gruhn, P., "Einfluss einer Heckklappe auf die Düsenströmung im Hyperschall," Ph.D. Dissertation, RWTH Aachen, Aachen, 2004.

[35] Herrmann, H., and Rick, H., "Propulsion Aspects of Hypersonic Turbo-Ramjet-Engines with Special Emphasis on Nozzle/Aftbody Integration," *International Gas Turbine and Aeroengine Congress and Exposition*, American Society of Mechanical Engineers, Fairfield, NJ, 1991.

R. Bowersox
Associate Editor